SIAM J. SCI. COMPUT.
Vol. 40, No. 1, pp. B259–B282

ACCURATE AND EFFICIENT NYSTRÖM VOLUME INTEGRAL EQUATION METHOD FOR ELECTROMAGNETIC SCATTERING OF 3-D METAMATERIALS IN LAYERED MEDIA*

DUAN CHEN†, MIN HYUNG CHO‡, AND WEI CAI§

Abstract. In this paper, we develop an accurate and efficient Nyström volume integral equation (VIE) method for the Maxwell equations to compute the electromagnetic scattering of three-dimensional metamaterials in layered media. The VIE for meta-atom scatterers in a layered medium is derived using dyadic Green's functions for layered media where Cauchy Principal Values are evaluated accurately using a finite-size exclusion volume with the help of some correction integrals of removable singularities. Several desingularization techniques are also introduced for the VIE, including interpolated quadrature formulas with tensor-product quadrature nodes for self-integration terms of typical meta-atoms, a regularization scheme for closely packed meta-atoms, and adaptive integration approaches for high gradient components of the dyadic Green's functions. The resulting Nyström method demonstrates fast numerical convergence with high accuracy and efficiency with only a small number of collocation points in calculating the scattered fields and reflection coefficients of metamaterials of cubic, spherical, and cylindrical shapes.

Key words. electromagnetic scattering, volume integral equation, metamaterials, Cauchy Principal Value, layered Green's function

AMS subject classifications. 65R20, 65Z05, 78M25

DOI. 10.1137/16M110900X

1. Introduction.

Metamaterials (MMs) are a type of composite materials fabricated using structured or random nanoscale objects (i.e., meta-atoms) in possibly layered media. Not found in nature, these artificially designed materials can achieve dramatic optical reflection and absorption properties and thus can be tailored to manipulate light waves for desired effective properties and functionalities. MMs have a wide range of applications, ranging from solar cells [4] to superresolution imaging devices [22, 15], in which the interaction of light with surface plasmons on roughened metallic surfaces produces surface plasmon polaritons [3, 23] and plays a critical role. In addition, surface-enhanced Raman scattering [24] is closely related to the excitation of surface plasmons on rough or nanopatterned surfaces by incident light and is a very useful tool in fingerprinting chemical components of a molecule, single-molecule detection, DNA detection, biosensing, etc. [16].

In a solar cell's absorber based on a metasurface, a typical constitutive structure corresponds roughly to an area of 100×100 nm^2 unit cell; a macroscopical area of 1 cm^2 on a solar cell gives 10^{10} degrees of freedom. Therefore, efficient computational

*Submitted to the journal's Computational Methods in Science and Engineering section December 21, 2016; accepted for publication (in revised form) September 26, 2017; published electronically February 7, 2018.

http://www.siam.org/journals/sisc/40-1/M110900.html

Funding: This work was supported by the U.S. Army Office of Research (grant W911NF-17-1-0368) and U.S. National Science Foundation (grant DMS-1802143). The first author's work was also supported by UNCC faculty research grant (2015-2017). The second author's work was supported by a grant from the Simons Foundation (404499).

†Department of Mathematics and Statistics, University of North Carolina at Charlotte, Charlotte, NC 28223 (dchen10@uncc.edu).

‡Department of Mathematical Sciences, University of Massachusetts Lowell, Lowell, MA 01854 (MinHyung_Cho@uml.edu).

§Corresponding author. Department of Mathematics, Southern Methodist University, Dallas, TX 75275 (cai@smu.edu).

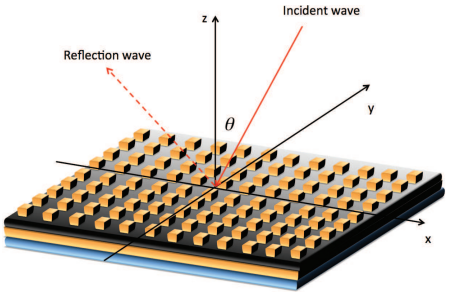

FIG. 1. *Illustration of light reflection on MMs.*

algorithms and optimization techniques are indispensable to bridging the macroscopic length scale of the solar cell absorber and the nanoscale of the underlying feature sizes. Due to the very-large-scale-integration technologies widely used in the fabrication process, MMs are composed of meta-atoms integrated into a layered background medium, such as in Figure 1. Numerous computational methods for electromagnetic (EM) scattering in inhomogeneous and layered media have been developed in past decades, including the finite element method [21] or the finite difference method [10, 29], with proper choices of perfectly matched layer boundary conditions [25, 27] and boundary integral equations for periodic scatterers [6, 7, 11]. The integral equation method is another popular method for computing scattering in layered media and requires the computation of dyadic Green's functions in terms of Sommerfeld integrals. Readers are referred to a recent review [20] and related literature therein.

In this paper, a volume integral equation (VIE) method for the EM scattering of MMs will be designed for such a layered structure where dielectric interface and radiation conditions at the infinite are accounted for through the layered dyadic Green's functions.

Our approach relies on the VIE representation for the solution of the time harmonic Maxwell equations with a dyadic layered Green's function $\overline{\mathbf{G}}_{\mathbf{E}}(\mathbf{r}, \mathbf{r}')$. To find the solution, the VIE is only discretized over the meta-atoms embedded in the layered media where the electric field will be found. Meanwhile, the EM field elsewhere can be available through the volume integral representation. The dyadic Green's function $\overline{\mathbf{G}}_{\mathbf{E}}(\mathbf{r}, \mathbf{r}')$ will ensure that the scattering field, expressed in terms of equivalent current sources inside the scatterer, satisfies interfacial conditions along horizontal layer interfaces as well as the Silver–Müller radiation conditions at infinity. The VIE method is especially suitable for computing EM scattering inside a large number of small meta-atoms in either a regular or a random distribution in layered materials.

However, numerically solving the VIE faces several difficulties due to the hypersingularity of the dyadic Green's function $\overline{\mathbf{G}}_{\mathbf{E}}(\mathbf{r}, \mathbf{r}')$, as we are required to calculate integrals of the form

$$\int_{\Omega_i} \mathrm{d}\mathbf{r}' \overline{\mathbf{G}}_{\mathbf{E}}(\mathbf{r}, \mathbf{r}')\phi(\mathbf{r}'), \tag{1}$$

where $\phi(\mathbf{r})$ is a smooth function and Ω_i is a meta-atom in the three-dimensional (3-D) space. Since the Green's function $\overline{\mathbf{G}}_{\mathbf{E}}(\mathbf{r}, \mathbf{r}')$ has an $O\left(\frac{1}{R^3}\right)$ singularity at $\mathbf{r} = \mathbf{r}' \in \Omega_i$, solving the VIE requires the use of the Cauchy Principal Value (CPV or simply p.v.) of (1), which calls for algorithms for their accurate and efficient computations. Various computational algorithms and analysis have been developed for this

Lippmann–Schwinger-type equation [1, 26, 31]. Especially, previous work on how to handle singular integrals for VIE methods include mixed potential formulation [14], singularity subtraction [18], locally corrected Nyström scheme [19], direct integration of the singularity [28], etc. Recently, a Nyström method based on interpolated quadrature weights [9] was developed to solve the VIE for multiple 3-D scatterers in a homogeneous medium with special interpolated quadrature weights [32]. Accuracy and efficiency of the VIE solution have been demonstrated for meta-atoms of some canonical geometries (cubes, spheres, and cylinders) in MMs.

There are still several outstanding issues in applying the algorithms in [9, 32] to VIE with layered Green's functions for general configurations of scatterers. First, the interpolated weights developed in [32] require an analytic expression for the integrand with (weak, strong, or hyper-) singularities while only numerical values of layered Green's functions are available. Second, the interpolated weights developed in [32] are designed for the case when both the source point $\mathbf{r}$ and the field point $\mathbf{r}'$ are located within the same scatterer. In realistic simulations of MMs, two meta-atoms, say, Ω_i and Ω_j, could be very close to each other. In such a case, it remains a big challenge to evaluate the integral in (1) for $\mathbf{r} \in \Omega_j$ since $\overline{\mathbf{G}}_{\mathbf{E}}(\mathbf{r}, \mathbf{r}')$ may have a large gradient even though it is a regular bounded function in the domain Ω_i. The naive approach of using large number of Gauss quadrature points to integrate the high gradient integrand will result in prohibitive computational cost, especially when a large number of meta-atoms are simulated. Finally, calculation of layered Green's function $\overline{\mathbf{G}}_{\mathbf{E}}(\mathbf{r}, \mathbf{r}')$ requires many Sommerfeld integrals and is also computationally costly.

We will develop computational techniques in this paper to tackle these difficulties. First, the layered Green's function will be decomposed into a singular and a regular part. The singular part resembles the analytic dyadic Green's function in the free space, which can be handled by the interpolated weights developed in [32]. On the other hand, the regular part will be computed using Sommerfeld integrals numerically, which has no singularity and thus can be handled with regular quadrature rules. Second, a regularization scheme, based on volume-to-surface integral conversions, is proposed to accurately calculate (1) with a small number of quadrature points when $\mathbf{r} \notin \Omega_i$ but close to Ω_i. Finally, an interpolating tabulation of the layered Green's function will be adopted, avoiding computing Sommerfeld integrals on the fly. This treatment is efficient for the simulation of a large number of meta-atoms.

The rest of the paper is organized as follows. Section 2 presents the VIE for the Maxwell equations in layered media under incident waves as well as a brief derivation (details are given in an appendix), formulation of the layered Green's function, and some analysis of the CPV of the VIE. Numerical methods are presented in section 3, consisting of the discretization of the VIE and different computational treatments of matrix entries. In section 4, accuracy and efficiency of the proposed algorithms are demonstrated. Finally, the paper ends with a conclusion in section 5.

2. Volume integral equation method.

2.1. VIE for the Maxwell equations in layered media. Consider an N_l-layered medium, labeled as $L_1 \sim L_{N_l}$ as shown in Figure 2, with the top layer as air. All the dielectric boundaries $S_1 \sim S_{N_l-1}$ are assumed to be parallel in the xy-plane, and the location of the top dielectric boundary S_1 is at $z = 0$. Permittivity and permeability for each layer are denoted as ϵ_i and μ_i, respectively. A 3-D scatterer

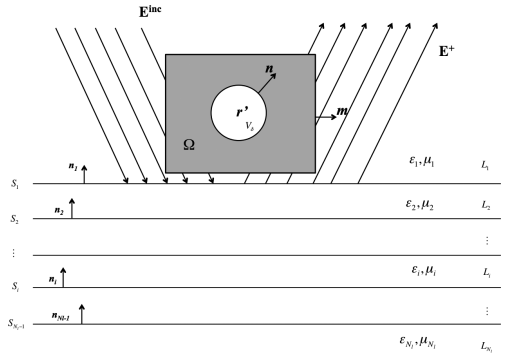

FIG. 2. *Illustration of a scatterer in a layered medium.*

Ω, placed in layer L_1 above S_1, is characterized by a different dielectric function $\varepsilon_1 + \Delta\epsilon(\mathbf{r})$. For any $\mathbf{r}' \in \Omega$, the dyadic Green's function $\overline{\mathbf{G}}_{\mathbf{E}}(\mathbf{r}, \mathbf{r}')$ is defined by

$$\mathcal{L}\overline{\mathbf{G}}_{\mathbf{E}}(\mathbf{r}, \mathbf{r}') - \omega^2 \epsilon_L(\mathbf{r}) \overline{\mathbf{G}}_{\mathbf{E}}(\mathbf{r}, \mathbf{r}') = \frac{1}{\mu(\mathbf{r})} \bar{\mathbf{I}} \delta(\mathbf{r} - \mathbf{r}'), \ \mathbf{r} \in \mathbb{R}^3, \tag{2}$$

where

$$\mathcal{L} = \nabla \times \frac{1}{\mu} \nabla \times, \qquad \epsilon_L(\mathbf{r}) = \varepsilon_i, \quad \mathbf{r} \in L_i, \tag{3}$$

ω is the frequency, $\delta(\mathbf{r} - \mathbf{r}')$ is the Dirac delta function, and $\bar{\mathbf{I}}$ is the unit dyad.

From some derivation given in the appendix, we obtain the following volume integral equation:

$$\begin{aligned} \mathbf{C} \cdot \mathbf{E}(\mathbf{r}) = \mathbf{E}^{\mathrm{src}}(\mathbf{r}) &+ \mu\omega^2 \ \text{p.v.} \int_\Omega \Delta\epsilon(\mathbf{r}') \mathbf{E}(\mathbf{r}') \cdot \overline{\mathbf{G}}^*_{\mathbf{E}}(\mathbf{r}, \mathbf{r}') d\mathbf{r}' \\ &+ \mu\omega^2 \int_\Omega \Delta\epsilon(\mathbf{r}') \mathbf{E}(\mathbf{r}') \cdot \overline{\mathbf{G}}^{\mathrm{reg}}_{\mathbf{E}}(\mathbf{r}, \mathbf{r}') d\mathbf{r}', \end{aligned} \tag{4}$$

where

$$\overline{\mathbf{G}}_{\mathbf{E}}(\mathbf{r}, \mathbf{r}') = \overline{\mathbf{G}}^*_{\mathbf{E}}(\mathbf{r}, \mathbf{r}') + \overline{\mathbf{G}}^{\mathrm{reg}}_{\mathbf{E}}(\mathbf{r}, \mathbf{r}') \tag{5}$$

with $\overline{\mathbf{G}}^*_{\mathbf{E}}(\mathbf{r}, \mathbf{r}')$ being the free space Green's function

$$\overline{\mathbf{G}}^*_{\mathbf{E}}(\mathbf{r}, \mathbf{r}') = \left(\bar{\mathbf{I}} + \frac{1}{k^2} \nabla\nabla \right) g(\mathbf{r}, \mathbf{r}') \tag{6}$$

and

$$g(\mathbf{r}, \mathbf{r}') = \frac{1}{4\pi} \frac{\mathrm{e}^{-\mathrm{i}kR}}{R}, \qquad R = |\mathbf{r} - \mathbf{r}'|. \tag{7}$$

The other part $\overline{\mathbf{G}}^{\mathrm{reg}}_{\mathbf{E}}(\mathbf{r}, \mathbf{r}')$ is nonsingular, and its definition is given in section 2.2.

The coefficient matrix on the left-hand side of (4) is given by $\mathbf{C} = \mathbf{I} + \mathbf{L}_{V_\delta} \cdot \Delta\epsilon(\mathbf{r})$, and the source term $\mathbf{E}^{\mathrm{src}}$ is

$$\begin{aligned} \mathbf{E}^{\mathrm{src}}(\mathbf{r}) = &\int_{\partial\Omega} \mathbf{m} \cdot \left(\mathbf{E}^{\mathrm{inc}} \times \nabla \times \overline{\mathbf{G}}_{\mathbf{E}} + \nabla \times \mathbf{E}^{\mathrm{inc}} \times \overline{\mathbf{G}}_{\mathbf{E}} \right) ds' \\ &+ \int_{S_1} \mathbf{n}_1 \cdot \left(\mathbf{E}^{\mathrm{inc}} \times \nabla \times \overline{\mathbf{G}}_{\mathbf{E}} + \nabla \times \mathbf{E}^{\mathrm{inc}} \times \overline{\mathbf{G}}_{\mathbf{E}} \right) ds', \end{aligned} \tag{8}$$

where $\mathbf{E}^{\text{inc}}$ is the given incident wave. Finally, the CPV in (4) is defined as

$$\text{p.v.} \int_\Omega \mathrm{d}\mathbf{r}'\ \Delta\epsilon(\mathbf{r}')\mathbf{E}(\mathbf{r}')\cdot\overline{\mathbf{G}}^*_{\mathbf{E}}(\mathbf{r}',\mathbf{r}) = \lim_{\delta\to 0}\int_{\Omega\setminus V_\delta} \mathrm{d}\mathbf{r}'\Delta\epsilon(\mathbf{r}')\mathbf{E}(\mathbf{r}')\cdot\overline{\mathbf{G}}^*_{\mathbf{E}}(\mathbf{r}',\mathbf{r}). \tag{9}$$

We have shown that the limit of the integral on the right-hand side can be computed with a finite δ associated with the help of some correction terms similar to [9, 14]. As a result, the VIE (4) becomes

$$\begin{aligned}\mathbf{C}\cdot\mathbf{E} = \mathbf{E}^{\text{src}}(\mathbf{r}) &+ \mu\omega^2\int_{\Omega\setminus V_\delta} d\mathbf{r}'\Delta\epsilon(\mathbf{r}')\mathbf{E}(\mathbf{r}')\cdot\overline{\mathbf{G}}^*_{\mathbf{E}}(\mathbf{r},\mathbf{r}') + \mu\omega^2\int_\Omega \mathrm{d}\mathbf{r}'\Delta\epsilon(\mathbf{r}')\mathbf{E}(\mathbf{r}')\cdot\overline{\mathbf{G}}^{\text{reg}}_{\mathbf{E}}(\mathbf{r},\mathbf{r}')\\ &+ \mu\omega^2\int_{V_\delta}\mathrm{d}\mathbf{r}'\Delta\epsilon(\mathbf{r}')\mathbf{E}(\mathbf{r}')\cdot\left(\overline{\mathbf{G}}^*_{\mathbf{E}}(\mathbf{r},\mathbf{r}') - \frac{1}{k^2}\nabla\nabla g_0\right)\\ &+ \frac{\mu\omega^2}{k^2}\int_{V_\delta}\mathrm{d}\mathbf{r}'\nabla\nabla g_0(\mathbf{r},\mathbf{r}')\left[\Delta\epsilon(\mathbf{r}')\mathbf{E}(\mathbf{r}') - \Delta\epsilon(\mathbf{r})\mathbf{E}(\mathbf{r})\right],\end{aligned} \tag{10}$$

where

$$g_0(\mathbf{r},\mathbf{r}') = \frac{1}{4\pi|\mathbf{r}-\mathbf{r}'|}. \tag{11}$$

Now the VIE (10) holds for any finite $\delta > 0$ as long as $V_\delta \subset \Omega$, and all the involved integrals are well-defined provided that $\Delta\epsilon(\mathbf{r})\mathbf{E}(\mathbf{r})$ is Hölder continuous. The last two terms in (10) can be understood as correction terms for computing the CPV with a finite-sized exclusion volume V_δ, and both are weakly singular integrals of removable singularities by a spherical coordinate transform of order $O(\delta^2)$[9].

Furthermore, calculations of the surface integrals on the surfaces S_1 and $\partial\Omega$ in (8) can be avoided for special incident waves. Note that the source term $\mathbf{E}^{\text{src}}$ has no dependence on the function $\Delta\epsilon(\mathbf{r})$. Therefore, if the incident wave is a plane wave and $\Delta\epsilon(\mathbf{r}) = 0$, the source term $\mathbf{E}^{\text{src}}$ can be found analytically, which remains the same for general nonzero $\Delta\epsilon(\mathbf{r})$. In fact, $\mathbf{E}^{\text{src}}$ is exactly the sum of the incident wave and its reflection by the layered medium. For example, for a two-layered medium with ϵ_1, ϵ_2 and $\mu_1 = \mu_2 = 1$, with a plane wave incident TE field $\mathbf{E}^{\text{inc}}(\mathbf{r}) = \hat{y}E_i\exp(-i\mathbf{k}_i\cdot\mathbf{r})$ with $\mathbf{k}_i = \omega(\hat{x}\sin\theta_i + \hat{z}\cos\theta_i)$ and θ_i as the incident angle, by Snell's law the transmission angle θ_t is determined by $\sqrt{\epsilon_1}\sin\theta_i = \sqrt{\epsilon_2}\sin\theta_t$, and by Fresnel's formula the reflective wave is $\mathbf{E}^r(\mathbf{r}) = \hat{y}r_sE_i\exp(-i\mathbf{k}_r\cdot\mathbf{r})$, where $\mathbf{k}_i = \omega(\hat{x}\sin\theta_i - \hat{z}\cos\theta_i)$ and $r_s = -\sin(\theta_i-\theta_t)/\sin(\theta_i+\theta_t)$. Finally, we have for plane incident waves

$$\begin{aligned}\mathbf{E}^{\text{src}}(\mathbf{r}) &= \int_{\partial\Omega}\mathbf{m}\cdot\left(\mathbf{E}^{\text{inc}}\times\nabla\times\overline{\mathbf{G}}_{\mathbf{E}} + \nabla\times\mathbf{E}^{\text{inc}}\times\overline{\mathbf{G}}_{\mathbf{E}}\right)ds'\\ &\quad+\int_{S_1}\mathbf{n}_1\cdot\left(\mathbf{E}^{\text{inc}}\times\nabla\times\overline{\mathbf{G}}_{\mathbf{E}} + \nabla\times\mathbf{E}^{\text{inc}}\times\overline{\mathbf{G}}_{\mathbf{E}}\right)ds'\\ &= \mathbf{E}^{\text{inc}}(\mathbf{r}) + \mathbf{E}^r(\mathbf{r}) = \hat{y}E_i\exp(-i\mathbf{k}_i\cdot\mathbf{r}) + \hat{y}r_sE_i\exp(-i\mathbf{k}_r\cdot\mathbf{r}).\end{aligned} \tag{12}$$

2.2. Dyadic Green's function in multilayered media. The dyadic Green's function is an essential component in the VIE for layered media. In [13], the dyadic Green's function for a two-layer material was derived, which has been recently extended to three layers in [12]. Consider a medium of three layers of dielectric materials with parameters $\varepsilon_i, \mu_i, i = 1, 2, 3$ and the two horizontal dielectric interface boundaries denoted as S_1 and S_2, respectively. For our applications we assume that all of the scatterers $\{\Omega_i\}$ are located within one layer and do not cross any dielectric boundary.

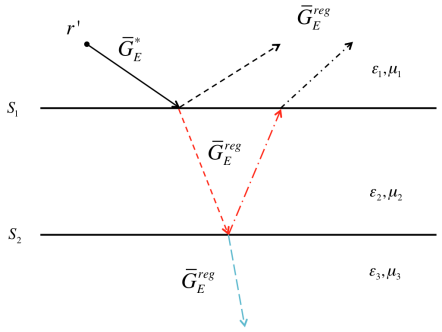

FIG. 3. *Illustration of the layered Green's function. Interfaces S_1 and S_2 separate three layers of materials with dielectric constant ε_i and permittivity μ_i $(i = 1, 2, 3)$. The overall layered Green's function is made of a primary, or singular, part and a regular part. Solid black lines represent the primary, or singular, part throughout all three layers. Dashed black lines are the regular part of the layered Green's function in the first layer, including the reflected part from S_1 and the transmitted part from the second layer. Red dashed lines are the regular part in the second layer, including the transmitted part from S_1 and the reflected part from S_1. Finally, the blue dashed line represents the regular part in the third layer, which is the transmitted field from the second layer.*

Within each scatterer, the primary, or singular, part $\overline{\mathbf{G}}_{\mathbf{E}}^{*}(\mathbf{r}, \mathbf{r}')$, is the Green's function in the free space defined in (6)–(7), and the remaining part is the regular part $\overline{\mathbf{G}}_{\mathbf{E}}^{\mathrm{reg}}(\mathbf{r}, \mathbf{r}')$, which is singularity free at $\mathbf{r} = \mathbf{r}'$. Figure 3 illustrates the components of the dyadic Green's function in the three layers, where the primary, or singular, part is represented by the black solid line and the regular, or reflected, part due to dielectric boundaries is shown as the two dashed black lines. In the second layer, the Green's function only contains a regular part, representing the transmitted field through boundary S_1 (dashed red line) and the reflected field from S_2 (dot-dashed red line). In the third layer, the Green's function only contains a regular part as the transmitted field through S_2 (the dashed blue line). Details of the derivation of layered Green's function can be found in [12]. Here, we list the case when the scatterers are in the first layer or when both source and field points are in the first layer.

In this situation, the regular part of the layered Green's function is the reflected fields from the lower two layers, which is given by

$$\overline{\mathbf{G}}_{\mathbf{E}}^{\mathrm{reg}}(\mathbf{r}, \mathbf{r}') = \overline{\mathbf{G}}_{1}^{R}(\mathbf{r}, \mathbf{r}') = -\frac{1}{8\pi^2\omega\varepsilon_0\varepsilon_1} \begin{pmatrix} G_{1,xx} & G_{1,xy} & G_{1,xz} \\ G_{1,yx} & G_{1,yy} & G_{1,yz} \\ G_{1,zx} & G_{1,zy} & G_{1,zz} \end{pmatrix}, \tag{13}$$

where

$$\begin{aligned} G_{1xx}^R &= -\frac{1}{2} g_{1,5}^R + \left(\frac{1}{2}\rho^2 - (y - y')^2\right) g_{1,6}^R, \\ G_{1yy}^R &= -\frac{1}{2} g_{1,5}^R - \left(\frac{1}{2}\rho^2 - (y - y')^2\right) g_{1,6}^R, \\ G_{1zz}^R &= g_{1,7}^R, \quad G_{1xy}^R = G_{1yx}^R = (x - x')(y - y') g_{1,6}^R, \\ G_{1xz}^R &= -G_{1zx}^R = -i(x - x') g_{1,8}^R, \\ G_{1yz}^R &= -G_{1zy}^R = -i(y - y') g_{1,8}^R, \end{aligned} \tag{14}$$

where $\rho = \sqrt{(x-x')^2 + (y-y')^2}$ and all the elements $g^R_{1,m}, m = 5, 6, 7, 8$ are defined in terms of Hankel integrals as

$$\tilde{g}^R_{1,5} = k_{1z}\bar{R}^{TM}_{12} - \frac{k_1^2}{k_{1z}}\bar{R}^{TE}_{12}, \quad \tilde{g}^R_{1,6} = \frac{k_{1z}\bar{R}^{TM}_{12}}{k_s^2} + \frac{k_1^2}{k_s^2 k_{1z}}\bar{R}^{TE}_{12},$$

$$\tilde{g}^R_{1,7} = \frac{k_s^2}{k_{1z}}\bar{R}^{TM}_{12}, \quad \tilde{g}^R_{1,8} = \bar{R}^{TM}_{12}, \tag{15}$$

and

$$\begin{aligned}
g^R_{1,5} &= 2\pi \int_0^\infty k_s \tilde{g}^R_{1,5} J_0(k_s\rho) e^{ik_{1z}(z+z')} dk_s, \\
g^R_{1,6} &= 2\pi \int_0^\infty k_s^3 \tilde{g}^R_{1,6} \frac{J_2(k_s\rho)}{\rho^2} e^{ik_{1z}(z+z')} dk_s, \\
g^R_{1,7} &= 2\pi \int_0^\infty k_s \tilde{g}^R_{1,7} J_0(k_s\rho) e^{ik_{1z}(z+z')} dk_s, \\
g^R_{1,8} &= 2\pi \int_0^\infty k_s^2 \tilde{g}^R_{1,8} \frac{J_1(k_s\rho)}{\rho} e^{ik_{1z}(z+z')} dk_s,
\end{aligned} \tag{16}$$

where $k_s^2 = k_x^2 + k_y^2$, $k_{lz} = \sqrt{k_l^2 - k_s^2}$, and J_n is the nth-order Bessel function. Definitions of the generalized reflection coefficients $\bar{R}^{TM,TE}_{12}$ and a general formulation of the layered Green's function can be found in [12, 13].

3. Numerical methods.

3.1. Discretization of the VIE. The computational domain Ω is assumed to be comprised of N nonoverlapping meta-atom elements Ω_i , $i = 1, 2, \ldots, N$. On each element Ω_i, we assign M tensor-product collocation nodes, for which M scalar interpolant Lagrange basis functions $\phi_{ij}, j = 1, 2, 3, \ldots, M$ are defined. Then we can write the solution as

$$\mathbf{E}(\mathbf{r}) = \sum_{i=1}^{N}\sum_{j=1}^{M} \mathbf{E}_{ij}\phi_{ij}(\mathbf{r}), \qquad \mathbf{r} \in \Omega_i, \tag{17}$$

where $\mathbf{E}_{ij}, 1 \le ij \le MN$ are the MN unknown vectorial nodal values of the numerical solution $\mathbf{E}(\mathbf{r})$ at the jth node $\mathbf{r}_{ij}$ in the element Ω_i. Inserting (17) into (10), we obtain the linear equations for $\mathbf{E}_{ij}$,

$$\begin{aligned}
\mathbf{C}\cdot\mathbf{E}_{ij} = \mathbf{E}^{\mathrm{src}}_{ij} &+ \omega^2\mu \sum_{n=1}^{N}\sum_{m=1}^{M} \left[\int_{\Omega_n \setminus V_{\delta_{ij}}} \mathrm{d}\mathbf{r}'\Delta\epsilon(\mathbf{r}')\overline{\mathbf{G}}^*_{\mathbf{E}}(\mathbf{r}_{ij},\mathbf{r}')\phi_{nm}(\mathbf{r}')\right]\cdot\mathbf{E}_{nm} \\
&+ \omega^2\mu \sum_{n=1}^{N}\sum_{m=1}^{M} \mathbf{E}_{nm}\cdot\left[\int_{\Omega_n} \mathrm{d}\mathbf{r}'\Delta\epsilon(\mathbf{r}')\overline{\mathbf{G}}^{\mathrm{reg}}_{\mathbf{E}}(\mathbf{r}_{ij},\mathbf{r}')\phi_{nm}(\mathbf{r}')\right] \\
&+ \omega^2\mu \sum_{m=1}^{M} \left[\int_{V_{\delta_{ij}}} \mathrm{d}\mathbf{r}'\Delta\epsilon(\mathbf{r}')\left(\overline{\mathbf{G}}^*_{\mathbf{E}}(\mathbf{r},\mathbf{r}') - \frac{1}{k^2}\nabla\nabla g_0\right)\phi_{im}(\mathbf{r}')\right]\cdot\mathbf{E}_{im} \\
&+ \frac{\mu\omega^2}{k^2}\sum_{m=1}^{M}\int_{V_{\delta_{ij}}} \mathrm{d}\mathbf{r}'\nabla^2 g_0(\mathbf{r}_{ij},\mathbf{r}')\left[\Delta\epsilon(\mathbf{r}')\phi_{im}(\mathbf{r}') - \Delta\epsilon_{ij}\phi_{im}(\mathbf{r}_{ij})\right]\cdot\mathbf{E}_{im},
\end{aligned} \tag{18}$$

or, in a matrix form,

$$\sum_{n=1}^{N}\sum_{m=1}^{M}(\mathbf{A}_{nm} + \mathbf{B}_{nm})\cdot\mathbf{E}_{nm} + \sum_{m=1}^{M}\mathbf{C}_{im}\cdot\mathbf{E}_{im} + \left(1 + \frac{1}{3}\Delta\epsilon_{ij}\right)\mathbf{I}_{3\times 3}\cdot\mathbf{E}_{ij} = \mathbf{E}^{\mathrm{src}}_{ij}, \tag{19}$$

where

$$\mathbf{A}_{nm} = -\omega^2\mu \int_{\Omega_n \setminus V_{\delta_{ij}}} \mathrm{d}\mathbf{r}' \Delta\epsilon(\mathbf{r}') \overline{\mathbf{G}}^*_{\mathbf{E}}(\mathbf{r}_{ij}, \mathbf{r}') \phi_{nm}(\mathbf{r}') \tag{20}$$

$$\mathbf{B}^T_{nm} = -\omega^2\mu \int_{\Omega_n} \mathrm{d}\mathbf{r}' \Delta\epsilon(\mathbf{r}') \overline{\mathbf{G}}^{\mathrm{reg}}_{\mathbf{E}}(\mathbf{r}_{ij}, \mathbf{r}') \phi_{nm}(\mathbf{r}') \tag{21}$$

and

$$\begin{aligned} \mathbf{C}_{im} = & -\omega^2\mu \int_{V_{\delta_{ij}}} \mathrm{d}\mathbf{r}' \Delta\epsilon(\mathbf{r}') g(\mathbf{r}_{ij}, \mathbf{r}') \phi_{im}(\mathbf{r}') \\ & - \frac{\omega^2\mu}{k^2} \int_{V_{\delta_{ij}}} \mathrm{d}\mathbf{r}' \Delta\epsilon(\mathbf{r}') \nabla\nabla \widetilde{g}(\mathbf{r}_{ij}, \mathbf{r}') \phi_{im}(\mathbf{r}') \\ & - \frac{\omega^2\mu}{k^2} \int_{V_{\delta_{ij}}} \mathrm{d}\mathbf{r}' \nabla^2 g_0(\mathbf{r}_{ij}, \mathbf{r}') \left[\Delta\epsilon(\mathbf{r}') \phi_{im}(\mathbf{r}') - \Delta\epsilon_{ij} \phi_{im}(\mathbf{r}_{ij}) \right]. \end{aligned} \tag{22}$$

Note that transpose of matrix $\mathbf{B}_{nm}$ is necessary since the dyadic $\overline{\mathbf{G}}^{\mathrm{reg}}_{\mathbf{E}}$ is not symmetric.

3.2. Computation of matrix entries. Calculating integrals in (20)–(22) for the matrix filling process is one of the most time-consuming tasks in solving the VIE. There are $O(N^2M^2)$ operations of calculating integrals (20)–(21), and the evaluation of correction terms (22) involves $O(NM^2)$ operations as the corrections take place locally. We denote the total numbers of quadrature nodes to evaluate integrals (20), (21), and (22) as M_A, M_B, and M_c, respectively.

Because the total number of meta-atom scatterers is large most of time, it is beneficial to use small number M for M_A, M_B, and M_C in each scatterer while maintaining satisfactory accuracy.

3.2.1. An efficient Nyström method with interpolated weights. When the source point $\mathbf{r}_{ij}$ is located in a scatterer Ω_n, a direct evaluation of (20) requires a very large number M_A ($\sim 10^6$) in order to obtain an accurate result for $\mathbf{A}_{nm}$ since the function $\overline{G}^*_{\mathbf{E}}(\mathbf{r}_{ij}, \mathbf{r}')$ is hypersingular at $\mathbf{r}' = \mathbf{r}_{ij}$[32]. This direct brute-force method will make computation prohibitively expensive even for a small number of collocation points. To overcome this difficulty, an efficient Nyström-type method was developed in [9] by choosing ϕ_{nm} as basis functions with Kronecker delta property, and a set of quadrature points coincide with the collocation points; i.e., $M_A = M$ are used. Consequently, calculation of (20) becomes a pointwise evaluation of the function $\Delta\epsilon(\mathbf{r}')\overline{\mathbf{G}}^*_{\mathbf{E}}(\mathbf{r}_{ij}, \mathbf{r}')$, i.e.,

$$\begin{aligned} \mathbf{A}_{nm} &= \int_{\Omega_n \setminus V_{\delta_{ij}}} \mathrm{d}\mathbf{r}' \Delta\epsilon(\mathbf{r}') \overline{\mathbf{G}}^*_{\mathbf{E}}(\mathbf{r}_{ij}, \mathbf{r}') \phi_{nm}(\mathbf{r}') \\ &\approx \sum_{n'm'=1}^{M} \tilde{w}^{ij}_{n'm'} \Delta\epsilon(\mathbf{r}_{n'm'}) \overline{\mathbf{G}}^*_{\mathbf{E}}(\mathbf{r}_{ij}, \mathbf{r}_{n'm'}) \phi_{nm}(\mathbf{r}_{n'm'}) \\ &= \tilde{w}^{ij}_{nm} \Delta\epsilon(\mathbf{r}_{nm}) \overline{\mathbf{G}}^*_{\mathbf{E}}(\mathbf{r}_{ij}, \mathbf{r}_{nm}), \end{aligned} \tag{23}$$

so the total operation is reduced to $O(NM)$. Furthermore, a set of specially designed interpolate quadrature weights $\tilde{w}^{ij}_{nm}$ in [32] can be used to handle the hypersingularity when the source point $\mathbf{r}_{ij}$ is in the scatterer Ω_i. In this approach, high accuracy of the

solution is maintained while the computational efficiency is greatly improved. This algorithm is summarized as follows [9]:

$$\mathbf{A}_{nm} = \mathbf{A}_{im} = \frac{1}{4\pi}\mathcal{J}_i \sum_{j=1}^{M} \Delta\epsilon_{im} \Big[\Big(f_m^0 \omega_{j,m}^{r,i} + f_m^1 \omega_{j,m}^{i} + f_m^2 \bar{\omega}_{j,m}^{i} + f_m^3 \tilde{\omega}_{j,m}^{i} \Big) \mathbf{I}_{3\times 3} + f_m^0 \Lambda_{j,m}^{r,i} + f_m^1 \Lambda_{j,m}^{i} + f_m^2 \bar{\Lambda}_{j,m}^{i} + f_m^3 \tilde{\Lambda}_{j,m}^{i} \Big], \tag{24}$$

where

$$f_m^0 = -i\frac{\sin(kR_m)}{R_m}, \quad f_m^1 = \cos(kR_m) - \frac{\sin(kR_m)}{kR_m},$$
$$f_m^2 = -i\frac{\cos(kR_m)}{k} + i\frac{\sin(kR_m)}{k^2 R_m}, \quad f_m^3 = -\frac{\cos(kR_m)}{k^2}, \tag{25}$$

$R_m = |\mathbf{r}_{ij} - \mathbf{r}_{im}|$, and $\mathcal{J}_i$ is the Jacobian from the reference domain to the physical domain Ω_i. Details of the formulations (24) and (25), as well as the interpolated weights $\omega_{j,m}^{r,i}$, $\omega_{j,m}^{i}$, $\bar{\omega}_{j,m}^{i}$, $\tilde{\omega}_{j,m}^{i}$, $\Lambda_{j,m}^{r,i}$, $\Lambda_{j,m}^{i}$,$\bar{\Lambda}_{j,m}^{i}$,and $\tilde{\Lambda}_{j,m}^{i}$, can be found in [9, 32].

When $i \neq n$, i.e., the source point $\mathbf{r}_{ij}$ is not in the element Ω_n, (20) becomes

$$\mathbf{A}_{nm} = \int_{\Omega_n} \mathrm{d}\mathbf{r}' \Delta\epsilon(\mathbf{r}') \overline{\mathbf{G}}_{\mathbf{E}}^{*}(\mathbf{r}_{ij}, \mathbf{r}') \phi_{nm}(\mathbf{r}'), \tag{26}$$

where the function $\overline{\mathbf{G}}_{\mathbf{E}}^{*}(\mathbf{r}_{ij}, \mathbf{r}')$ is not singular in Ω_n, and hence no CPV treatment is needed. Generally, the $M_A (= M)$ Gaussian points $\mathbf{r}_{nm}$ in Ω_n with the corresponding weights ω_{nm} can be used. Then we have

$$\begin{aligned} \mathbf{A}_{nm} &= \int_{\Omega_n} \mathrm{d}\mathbf{r}' \Delta\epsilon(\mathbf{r}') \overline{\mathbf{G}}_{\mathbf{E}}^{*}(\mathbf{r}_{ij}, \mathbf{r}') \phi_{nm}(\mathbf{r}') \\ &\approx \sum_{n'm'=1}^{M} \omega_{n'm'} \Delta\epsilon(\mathbf{r}_{n'm'}) \overline{\mathbf{G}}_{\mathbf{E}}^{*}(\mathbf{r}_{ij}, \mathbf{r}_{n'm'}) \phi_{nm}(\mathbf{r}_{n'm'}) \\ &= \omega_{nm} \Delta\epsilon(\mathbf{r}_{nm}) \overline{\mathbf{G}}_{\mathbf{E}}^{*}(\mathbf{r}_{ij}, \mathbf{r}_{nm}), \end{aligned} \tag{27}$$

where ω_{nm} are the regular Gaussian quadrature weights.

3.2.2. A regularization scheme for close neighboring scatterers. When Ω_i is a close neighbor to Ω_n, the function $\overline{\mathbf{G}}_{E}^{*}(\mathbf{r}_{ij}, \mathbf{r}')$ is not singular in Ω_n if $\mathbf{r}_{ij} \in \Omega_i$, but it will have large derivatives. Thus, calculation of the matrix $\mathbf{A}_{nm}$ by (27) may lead to a low accuracy. One way to address this issue is to oversample with more Gaussian points to improve the accuracy at the expense of causing a large increase in computational time. Here, we propose a regularization scheme for spherical and cubic scatterers to keep the simple form of (27) while maintaining high accuracy.

For illustration, we consider the integral

$$\begin{aligned} \int_{\Omega} \mathrm{d}\mathbf{r}' \overline{\mathbf{G}}_{\mathbf{E}}^{*}(\mathbf{r}, \mathbf{r}') \phi(\mathbf{r}') &= \int_{\Omega} \mathrm{d}\mathbf{r}' \left\{ \bar{\mathbf{I}} g(\mathbf{r}, \mathbf{r}') + \frac{1}{k^2} \nabla^2 \left[g(\mathbf{r}, \mathbf{r}') - g_0(\mathbf{r}, \mathbf{r}') \right] \right\} \phi(\mathbf{r}') \\ &\quad + \int_{\Omega} \mathrm{d}\mathbf{r}' \nabla^2 g_0 [\phi(\mathbf{r}') - \phi(\mathbf{r}^*)] + \phi(\mathbf{r}^*) \int_{\Omega} \mathrm{d}\mathbf{r}' \nabla^2 g_0, \end{aligned} \tag{28}$$

where $\mathbf{r}^* \in \Omega$ is a point chosen to be close to the source point $\mathbf{r}$.

The integrand of the integral on the left-hand side of (28) is of $O(1/R^3)$ around the point $\mathbf{r}$. However, on the right-hand side, the first and second integrands are of $O(1/R)$ and $O(1/R^2)$, respectively, provided that $\mathbf{r}^*$ is close to $\mathbf{r}$. Thus, it is easier to obtain accurate results for these two integrals. Analytical evaluation can be carried out for the last integral in (28) for canonical geometries of meta-atoms, such as cubes and spheres. Therefore, decomposition of the integrals as in (28) will give better accuracy than directly computing the left-hand side.

Using the Gauss–Green theorem, we have

$$\int_\Omega \mathrm{d}\mathbf{r}'\nabla^2 g_0 = \int_{\partial\Omega} \mathrm{d}s\nabla g_0 \otimes \vec{n} = \int_{\partial\Omega} \mathrm{d}s \frac{\mathbf{r}-\mathbf{r}'}{4\pi R^3} \otimes \vec{n}. \tag{29}$$

For cubic scatterers: When the scatterer Ω is a cube $[x_0, x_1] \times [y_0, y_1] \times [z_0, z_1]$, the last integral in (29) becomes

$$\int_{\partial\Omega} \mathrm{d}s\nabla g_0 \otimes \vec{n} = \begin{pmatrix} \int_{\partial\Omega} \frac{x-x'}{R^3} dy'dz', & \int_{\partial\Omega} \frac{x-x'}{R^3} dx'dz', & \int_{\partial\Omega} \frac{x-x'}{R^3} dx'dy' \\ \int_{\partial\Omega} \frac{y-y'}{R^3} dy'dz', & \int_{\partial\Omega} \frac{y-y'}{R^3} dx'dz', & \int_{\partial\Omega} \frac{y-y'}{R^3} dx'dy' \\ \int_{\partial\Omega} \frac{z-z'}{R^3} dy'dz', & \int_{\partial\Omega} \frac{z-z'}{R^3} dx'dz', & \int_{\partial\Omega} \frac{z-z'}{R^3} dx'dy' \end{pmatrix}. \tag{30}$$

Denote (u, v, w) as an arbitrary permutation of the coordinates of point (x, y, z); then the nine integrals in (30) can be represented as two types of integrals as

$$\int_{\partial\Omega} \frac{u-u'}{R^3} dv'dw' = \int_{w_0}^{w_1}\int_{v_0}^{v_1} \frac{u-u'}{R^3}\bigg|_{u'=u_1} dv'dw' - \int_{w_0}^{w_1}\int_{v_0}^{v_1} \frac{u-u'}{R^3}\bigg|_{u'=u_0} dv'dw' \tag{31}$$

and

$$\int_{\partial\Omega} \frac{u-u'}{R^3} du'dv' = \int_{v_0}^{v_1}\int_{u_0}^{u_1} \frac{u-u'}{R^3}\bigg|_{w'=w_1} du'dv' - \int_{v_0}^{v_1}\int_{u_0}^{u_1} \frac{u-u'}{R^3}\bigg|_{w'=w_0} du'dv'. \tag{32}$$

Using Mathematica, it is easy to obtain

$$\int\int \frac{u-u'}{R^3} dw'dv' = \mathrm{Im}\left(\ln\left[-\frac{4(w-w'+R)(u-u')}{u-u'-i(v-v')} - \frac{4(u-u')^2}{w-w'}\right]\right) \tag{33}$$

and

$$\int\int \frac{u-u'}{R^3} du'dv' = -\ln(R+v-v'). \tag{34}$$

Thus, integral (29) can be evaluated exactly by (30)–(34).

For spherical scatterers: When Ω is a ball of radius a, due to the rotational symmetry, we can assume $\mathbf{r} = (0, 0, \rho)$ for convenience and use spherical coordinate $\mathbf{r}' = a(\sin\theta\cos\phi, \sin\theta\sin\phi, \cos\theta)$. Note

$$R = \sqrt{a^2\sin^2\theta + (a\cos\theta - \rho)^2} = \sqrt{a^2 + \rho^2 - 2a\rho\cos\theta} \tag{35}$$

and $\vec{n} = (\sin\theta\cos\phi, \sin\theta\sin\phi, \cos\theta)$; then (29) turns into

$$\int_{\partial\Omega} \mathrm{d}s\nabla g_0 \otimes \vec{n} = \int_0^{2\pi}\int_0^{\pi} \mathbf{A}_{3\times 3} d\theta d\phi, \tag{36}$$

where

$$\mathbf{A}_{3\times 3} = \begin{pmatrix} \frac{a^3\sin^3\theta\cos^2\phi}{R^3}, & \frac{a^3\sin^3\theta\cos\phi\sin\phi}{R^3}, & \frac{a^3\sin^2\theta\cos\theta\cos\phi}{R^3} \\ \frac{a^3\sin^3\theta\cos\phi\sin\phi}{R^3}, & \frac{a^3\sin^3\theta\sin^2\phi}{R^3}, & \frac{a^3\sin^2\theta\cos\theta\sin\phi}{R^3} \\ \frac{a^2\sin^2\theta\cos\phi(a\cos\theta-\rho)}{R^3}, & \frac{a^2\sin^2\theta\sin\phi(a\cos\theta-\rho)}{R^3}, & \frac{a^2\sin\theta\cos\theta(a\cos\theta-\rho)}{R^3} \end{pmatrix}. \tag{37}$$

It is easy to check from (37) that the matrix in (36) is diagonal, so we only need to handle two types of integrals appearing in the diagonal position of (37):

$$\int_0^\pi \frac{a^3\sin^3\theta}{R^3}d\theta \quad \text{and} \quad \int_0^\pi \frac{a^2\sin\theta\cos\theta(a\cos\theta-\rho)}{R^3}d\theta. \tag{38}$$

These integrals can be evaluated as, if $\lambda = \rho/a$,

$$\begin{aligned}\int_0^\pi \frac{a^3\sin^3\theta}{R^3}d\theta &= \int_0^\pi \frac{1-\cos^2\theta}{(\lambda^2-2\lambda\cos\theta+1)^{3/2}}d(\cos\theta) = \int_1^{-1}\frac{1-x^2}{(\lambda^2-2\lambda x+1)^{3/2}}dx \\ &= \frac{\lambda^2(x^2-1)+2(\lambda^3+\lambda)x-2\lambda^4-2}{3\lambda^3\sqrt{\lambda^2+1-2\lambda x}}\Big|_1^{-1} \end{aligned} \tag{39}$$

and

$$\begin{aligned}\int_0^\pi \frac{a^2\sin\theta\cos\theta(a\cos\theta-\rho)}{R^3}d\theta &= \int_0^\pi \frac{\cos^2\theta-\lambda\cos\theta}{(\lambda^2-2\lambda\cos\theta+1)^{3/2}}d(\cos\theta) \\ &= \int_1^{-1}\frac{x^2-\lambda x}{(\lambda^2-2\lambda x+1)^{3/2}}dx \\ &= -\frac{\lambda^2(x^2-1)+(2\lambda-\lambda^3)x+\lambda^4-2}{3\lambda^3\sqrt{\lambda^2+1-2\lambda x}}\Big|_1^{-1}. \end{aligned} \tag{40}$$

Based on (39)–(40), intergal (29) can be exactly computed from (36)–(37).

For other geometries, such as cylinders studied in [9], it may be difficult to find the analytic formula for the right-hand side of (29). For those cases, we have to use $M_A > M$ for close neighbors in order to obtain desired accuracy.

3.2.3. Computation of coefficients $\mathbf{B}_{nm}$ and $\mathbf{C}_{im}$. Since the regular part $\overline{\mathbf{G}}_{\mathbf{E}}^{\mathrm{reg}}(\mathbf{r}_{ij},\mathbf{r}')$ is singularity free, (21) can be carried out in a similar way as (27), namely,

$$\begin{aligned}\mathbf{B}_{nm} &= \int_{\Omega_n} \mathrm{d}\mathbf{r}'\Delta\epsilon(\mathbf{r}')\overline{\mathbf{G}}_{\mathbf{E}}^{\mathrm{reg}}(\mathbf{r}_{ij},\mathbf{r}')\phi_{nm}(\mathbf{r}') \\ &\approx \sum_{n'm'=1}^{M_B}\omega_{n'm'}\Delta\epsilon(\mathbf{r}_{n'm'})\overline{\mathbf{G}}_{\mathbf{E}}^{\mathrm{reg}}(\mathbf{r}_{ij},\mathbf{r}_{n'm'})\phi_{nm}(\mathbf{r}_{n'm'}). \end{aligned} \tag{41}$$

Generally, when the source point $\mathbf{r}_{ij}$ is fairly far away from the planar dielectric interfaces, we can take $M_B = M$; then the evaluation of (41) becomes a pointwise calculation $\omega_{nm}\Delta\epsilon(\mathbf{r}_{nm})\overline{\mathbf{G}}_{\mathbf{E}}^{\mathrm{reg}}(\mathbf{r}_{ij},\mathbf{r}_{nm})$. Unfortunately, when $\mathbf{r}_{ij}$ is very close to a planar interface, using $M_B = M$ will yield low accuracy. Moreover, no regularization scheme is available. In this case, we just take $M_B > M$ adaptively to ensure a satisfactory accuracy.

Another challenge in (41) is that of computing the regular part of layered Green's function $\overline{\mathbf{G}}_{\mathbf{E}}^{\mathrm{reg}}(\mathbf{r},\mathbf{r}')$ numerically through the Sommerfeld integral for each pair of $(\mathbf{r},\mathbf{r}')$. It is not practical to perform these computations on the fly, which requires

$O(N^2M^2M_B)$ Sommerfeld integrals. To tackle this issue, tables of values of integrals (16) are precalculated and stored for a fixed grid, and interpolations of the values on the grid are used for other collocation points in the VIE solution.

Finally, computing $\mathbf{C}_{im}$ in (22) is straightforward since the integrands have at most $O(\frac{1}{|\mathbf{r}-\mathbf{r}'|^2})$ singularity. Thus, a spherical coordinate transform can eliminate the singularity, and the number M_c does not need to be large.

4. Numerical results. We will present three sets of numerical tests on the proposed VIE. First, the efficiency and accuracy of the interpolation scheme for the layered dyadic Green's function are examined. Second, we test the numerical convergence of the VIE solutions for a single scatterer in layer media. Finally, we demonstrate the capability of the proposed method to calculate the reflection property of several MMs made of cubic, spherical, and cylindrical meta-atoms in layered media.

4.1. Accuracy and efficiency of interpolating layered Green's function. Fast matrix filling is much needed since it contributes major CPU time in the VIE method. When calculating the coefficient in (20), as the Green's function in free space $\overline{\mathbf{G}}^*_{\mathbf{E}}(\mathbf{r}_{ij}, \mathbf{r}')$ has an analytic formula and related interpolated weights are precalculated, the time spent in calculating (24)–(27) is not a big concern, and details for this step can be found in [9]. In contrast, calculating (21), involving the regular part of the layered Green's function $\overline{\mathbf{G}}^{\text{reg}}_{\mathbf{E}}(\mathbf{r}_{ij}, \mathbf{r}')$, requires expensive numerical computation of the Sommerfeld integral for each pair of source and field points. As mentioned above, the regular part will be precalculated and stored for a fixed set of grid points, and interpolated values can be then used for arbitrary points later.

According to (14), only the integrals $g^R_{1,m}$ defined by (16) need to be interpolated in terms of the variables $z + z'$ and ρ, respectively. Figure 4 shows the graphs of the integrals $g^R_{1,5}$, $g^R_{1,6}$, and $g^R_{1,7}$ in the domain $(0, 3\lambda] \times [0, 6\lambda]$ along z and ρ directions, respectively, where $\lambda = 2\pi/\omega$. These integrals take large values as $z + z' \to 0$ and $\rho = 0$ and decay rapidly otherwise.

To test the accuracy of the interpolations, we take $\lambda = 1$ and place a unit dipole α oriented in the direction $(\sin\frac{\pi}{18}\cos\frac{\pi}{18}, \sin\frac{\pi}{18}\sin\frac{\pi}{18}, \cos\frac{\pi}{18})$ at $(x', y', z') = (0, 0, 0.01)$, and the resulting field $\mathbf{E} = \alpha \cdot \overline{\mathbf{G}}_{\mathbf{E}}$ is calculated with the original and the interpolated regular part. The pointwise relative errors of the electric field $\mathbf{E}$ calculated by the two methods at $z' = 0.01$ and interpolation resolution $(\Delta\rho, \Delta z) = (0.2, 0.05)$, $(0.1, 0.025), (0.05, 0.0125)$ decrease from 4.0×10^{-2} to 4.6×10^{-3} and to 6.2×10^{-4}.

Matrix filling CPU time (in seconds) for the VIE is compared between on-the-fly and interpolation computation of layered Green's function in Table 1. For this case, a single cube ($N = 1$) and 27 collocation points ($M = 27$) are used. When calculating integral (41), the number of quadrature points $M_B = 3, 4, 5, 7$, and 16 are used to show the improvement in CPU time.

From the table we can see that direct calculation of the layered Green's function on the fly is computationally very expensive: Even with parallelization, it takes minutes for $M_B = 3, 4, 5, 6, 7$ and hours for $M_B = 16$. In later numerical results, we will see that the solution of VIE would not converge until $M_B = 16$. Therefore, it is necessary in practice to use interpolated layered Green's function in order to obtain accurate solutions within a reasonable time.

4.2. Validation of VIE method in layered media.

- Accuracy of dyadic Green's functions in layered media

In order to validate the formula for the layered Green's functions, we exam its limiting behavior when it approaches the Green's function in free space, i.e., $\varepsilon_2 = \varepsilon_3 \to \varepsilon_1$.

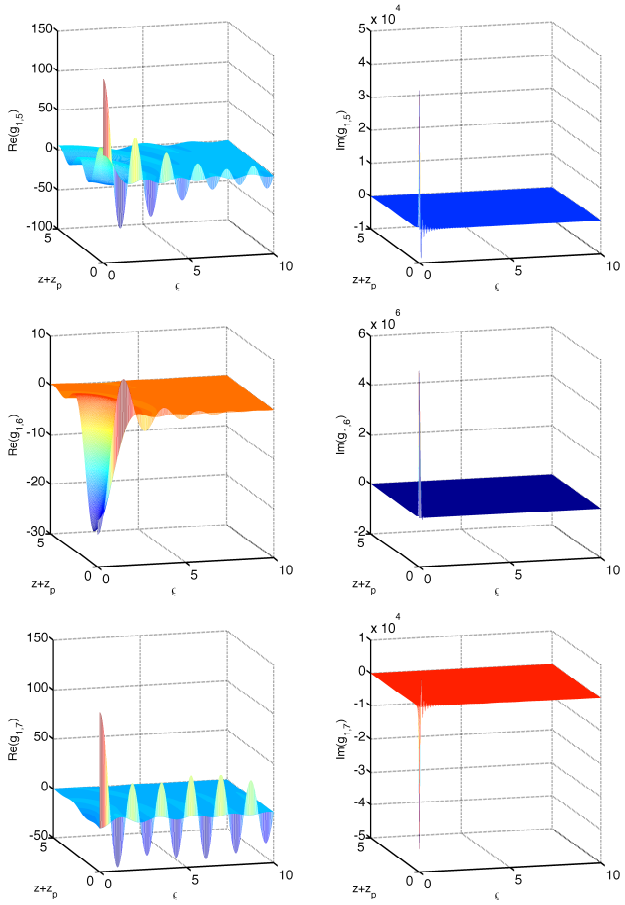

FIG. 4. *Behaviors of the Hankel integrals used in the layered Green's function. From top to bottom are for the integrals* $g^R_{1,5}$, $g^R_{1,6}$, *and* $g^R_{1,7}$. *The left panel is the real part, and the right panel is the imaginary part.*

TABLE 1

Comparison of matrix filling time (seconds) in solving VIE with the original and interpolated layered Green's function.

M_B	3	4	5	6	7	16
Original	52	127	247	417	677	7606
Interpolated	0.0123	0.018	0.03	0.045	0.0608	0.86

A unit dipole α is located at $\mathbf{r}' = (0, 0, 0.01)$ and oriented in the direction $(\sin\frac{\pi}{18}\cos\frac{\pi}{6}, \sin\frac{\pi}{18}\sin\frac{\pi}{6}, \cos\frac{\pi}{18})$; the electric field $\mathbf{E}(\mathbf{r}) = \alpha\cdot\overline{\mathbf{G}}_{\mathbf{E}}(\mathbf{r}, \mathbf{r}')$ with the choices of $\varepsilon_1 = 1, \varepsilon_2 = \varepsilon_3 = 1.1, 1.01, 1.001$, and 1.0001 will be compared with the field $\mathbf{E}'(\mathbf{r}) = \alpha\cdot\overline{\mathbf{G}}^*_{\mathbf{E}}(\mathbf{r}, \mathbf{r}')$, where $\overline{\mathbf{G}}^*_{\mathbf{E}}$ is the free space Green's function with $\varepsilon_0 = 1$. Figure 5 shows the limiting behavior of the difference $|\mathbf{E} - \mathbf{E}'|$ in E_x, E_y, and E_z at $(x, 0, 0.01)$ in (a)–(c), respectively. In these results, we take $\lambda = 1$, and the x-coordinate of $\mathbf{r}$ varies from -6 to 6, while y and z are fixed at $y = 0$ and $z = 0.01$, respectively. It can be concluded that as ε_2 and ε_3 tends to ε_1, the electric field tends to that generated by the free space Green's function. The imaginary part of the electric field has a similar limiting behavior.

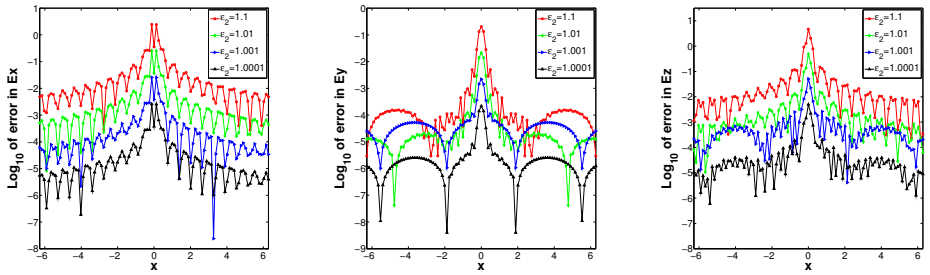

(a) (b) (c)

FIG. 5. *Limiting behavior of the layered Green's function. Electric field generated by a unit dipole located at* $(0, 0, 0.01)$ *and oriented in the direction* $(\sin\frac{\pi}{18}\cos\frac{\pi}{6}, \sin\frac{\pi}{18}\sin\frac{\pi}{6}, \cos\frac{\pi}{18})$. *Differences between the electric fields with the layered Green's function and with the free space Green's function are plotted.* (a) E_x; (b) E_y; (c) E_z.

TABLE 2
Error of regular part of layered Green's function in the Maxwell equation.

Component	$h = 0.8$	$h = 0.4$	$h = 0.2$	$h = 0.1$
$\left(\overline{\mathbf{G}}_{\mathbf{E}}^{\mathrm{err}}\right)_{xx}$	4.92E-3	1.60E-4	2.95E-5	1.20E-5
$\left(\overline{\mathbf{G}}_{\mathbf{E}}^{\mathrm{err}}\right)_{yy}$	4.95E-3	1.63E-4	2.91E-5	1.19E-5
$\left(\overline{\mathbf{G}}_{\mathbf{E}}^{\mathrm{err}}\right)_{zz}$	4.93E-3	1.66E-4	2.98E-5	1.10E-5

Another way to validate the results of the Green's functions is to check whether the nonsingular part of the layered Green's function satisfies the homogeneous Maxwell equation. The error matrix

$$\overline{\mathbf{G}}_{\mathbf{E}}^{\mathrm{err}} = \mathcal{L}\overline{\mathbf{G}}_{\mathbf{E}}^{\mathrm{reg}}(\mathbf{r}, \mathbf{r}') - \omega^2 \epsilon_L(\mathbf{r})\overline{\mathbf{G}}_{\mathbf{E}}^{\mathrm{reg}}(\mathbf{r}, \mathbf{r}') \tag{42}$$

is calculated, and the modulus of diagonal entries is listed in Table 2. In the computation, standard finite difference with discretization step lengths $h = 0.8, 0.4, 0.2,$ and 0.1 are used to approximate the differential operator. The source and field points are taken as $\mathbf{r} = \mathbf{r}' = (0, 0, 1)$. Dielectric constants are taken as $\epsilon_1 = 1$ and $\epsilon_2 = 4$, and the wavenumber is $k = 1$. The errors decrease in the same order of the central difference scheme, validating the accuracy of the computed Green's functions.

The accuracy can also the checked by examining the continuity of layered Green's function at interfaces, as done in [12].

- Validation of VIE method for scattering of a sphere over the half-space

Next, we solve the VIE with $\varepsilon_2 = \varepsilon_3 \to \varepsilon_1$ in a unit sphere placed on top of a layered medium and compare the solution $\mathbf{E}(\mathbf{r})$ to the analytic Mie solution $\mathbf{E}^{\mathrm{Mie}}(\mathbf{r})$ [9] in the free space. In this test, we set the parameters $\omega = 1$, $\varepsilon_1 = 1$, and $\varepsilon_2 = \varepsilon_3 = 10, 1.01,$ and 1.0001. The differences $|\mathbf{E}(\mathbf{r}) - \mathbf{E}^{\mathrm{Mie}}(\mathbf{r})|$ are shown pointwisely for coordinates (r, θ, ϕ) of the collocation points in Figure 6. As the layered Greens' function tends to the free space Green's function, the electric field tends to the Mie solution.

The total electric field, both inside and outside of a ball of radius 0.5 on top of a dielectric boundary, is given in Figure 7. In this case, we take the incident wave $\mathbf{E}^{\mathrm{inc}} = \mathbf{i}_y e^{i(\sqrt{2}x - \sqrt{2}z)}$ and $\varepsilon_1 = 1, \varepsilon_2 = \varepsilon_3 = 4$, wavelength $\lambda = 3$. The real part of the

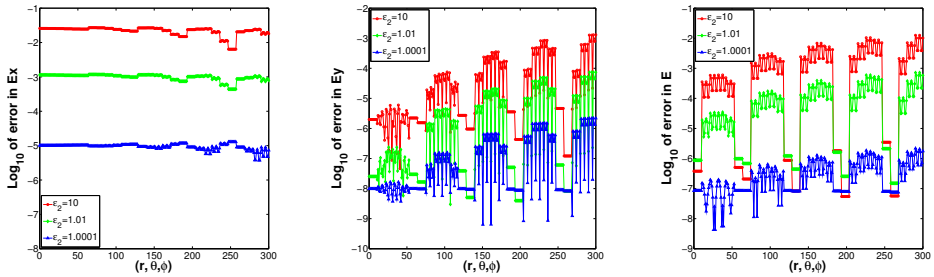

(a) (b) (c)

FIG. 6. *Asymptotic behavior of electric field in a unit sphere. Differences between the VIE solutions with the layered Green's function and with the free space Green's function are plotted.* (a) E_x; (b) E_y; (c) E_z.

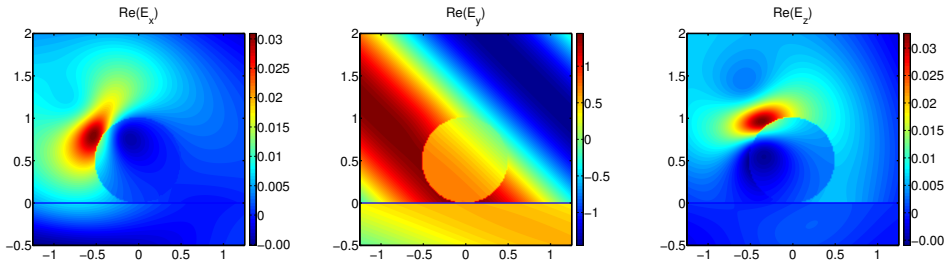

(a) (b) (c)

FIG. 7. *Electric field components* E_x (a), E_y (b), *and* E_z (c) *in a ball of radius* 0.5 *on top of a dielectric boundary.*

electric field at $y = 0$ for the domain $(x, z) = [-1.5, 1.5] \times [-0.5, 2]$ is plotted in a 2-D contour. The dielectric boundary is marked as the blue line at $z = 0$.

- Validation of VIE method for scattering of a cube on the half-space

Next, we check the accuracy of the quadrature rule when the scatterer is near the dielectric boundary. The VIE method is used to compute the scattering of a cube of size 2 on top of a dielectric medium with $\varepsilon_1 = 1$ and $\varepsilon_2 = \varepsilon_3 = 10$. The accuracy of its solution is measured by the L_2 relative error:

$$\text{Error} = \frac{\|\mathbf{E}^p - \mathbf{E}^{\text{ref}}\|_{L_2(\Omega)}}{\|\mathbf{E}^{\text{ref}}\|_{L_2(\Omega)}}, \tag{43}$$

where $\mathbf{E}^p$ is the numerical solution of the VIE with p collocation points in each coordinate direction and $\mathbf{E}^{\text{ref}}$ is a reference solution. The L_2 norm integral is discretized with the quadrature formula used in the VIE. In the tests, we take incident wave $\mathbf{E}^{\text{inc}} = \mathbf{i}_x e^{i(2y+2z)}$ and use $\mathbf{E}^7$ with $M_A = 7^3$ and $M_B = 16^3$ as the reference solution.

Figure 8 displays convergence of electric field $\mathbf{E}^p$ computed with collocation point per coordinate direction $p = 3, 4, 5, 6$. First we take $M_A = M_B = M = p^3$, and the convergence of the VIE solution in free space is shown in red for reference. When the cubic scatterer is $\frac{1}{6}\lambda$ away from the dielectric boundary at $z = 0$, a similar convergence pattern is obtained, as shown in the green curves with diamond points. However, when the scatterer is right on top of the dielectric boundary, no convergence is achieved even with $M_B = 7^3$ for $p = 3, 4, 5, 6$, as shown by the black dashed curve.

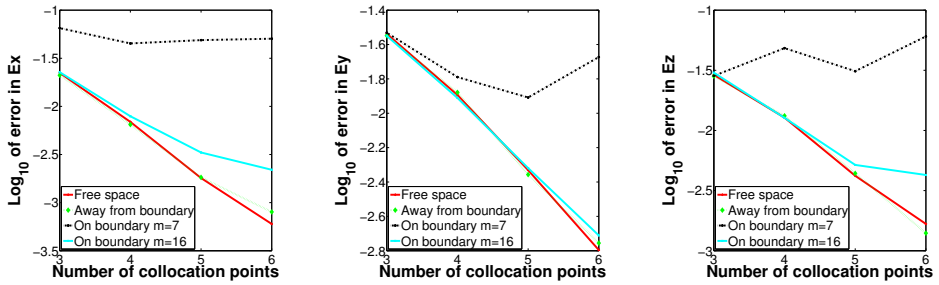

(a) E_x (b) E_y (c) E_z

FIG. 8. *Convergence of electric field* E^p *in a cubic scatterer in a layered medium.* $\log_{10}$ *errors agains number of collocation points in one direction.*

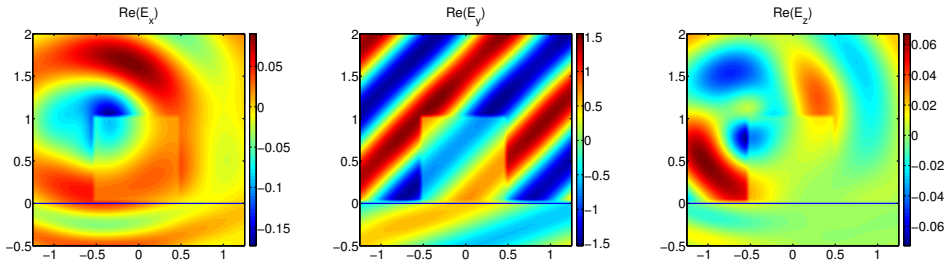

(a) (b) (c)

FIG. 9. *Electric field components* (a) E_x,(b) E_y, *and* (c) E_z *in a unit cube on top of a dielectric boundary.*

However, numerical convergence is obtained when we take $M_B = 16^3$. This test shows that, in order to achieve solutions with a reliable accuracy, we have to take $M_B = 16^3$ for this incident wave when the scatterers are sitting right on top of the dielectric boundary. With the CPU time shown in Table 1, it is clear that we have to use the procedure of interpolating the Green's function for realistic computation time.

In an additional case where $\varepsilon_1 = 1, \varepsilon_2 = \varepsilon_3 = 6$ and $\mathbf{E}^{\mathrm{inc}} = \mathbf{i}_y e^{i(-3\sqrt{2}x - 3\sqrt{2}z)}$, the total electric field, both inside and outside of a unit cube on top of a dielectric boundary, is given in Figure 9. In this case the wavelength $\lambda = 1$, and the real part of the electric field at $y = 0$ for the domain $(x, z) = [-1.5, 1.5] \times [-0.5, 2]$ is plotted in a 2-D contour. The dielectric boundary is marked as the blue line at $z = 0$.

4.3. EM scattering for MMs of multiple meta-atoms. First, we will show that the regularization scheme enhances the accuracy and efficiency of calculating integral in (26) when a source point $\mathbf{r}^s$ is outside of Ω but very close to it. In these tests, the computational domain Ω is taken as a cube of unit length, the coordinate of the source point $\mathbf{r}^s$ is $(-0.112702, 0.112702, 0.112702)$, and the coordinate of the first collocation point $\mathbf{r}_{11}$ is $(0.112702, 0.112702, 0.112702)$. This is a case in which two cubes Ω_i and Ω_j are adjacent to each other. We consider the integral

$$\begin{pmatrix} g_{11}, & g_{12}, & g_{13} \\ g_{21}, & g_{22}, & g_{23} \\ g_{31}, & g_{32}, & g_{33} \end{pmatrix} = \int_{\Omega} \mathrm{d}\mathbf{r}' \overline{\mathbf{G}}^*_{\mathbf{E}}(\mathbf{r}^s, \mathbf{r}') \phi_{11}(\mathbf{r}'), \tag{44}$$

where $\phi_{11}(\mathbf{r})$ is the basis function associated with the point $\mathbf{r}_{11}$.

TABLE 3

Comparison of accuracy between evaluating integral by direct Gauss quadrature and the regularization scheme. Reference solution: $g_{11} = 0.185619291$.

M_A	Direct integration	Error	Regularization	Error
3^3	0.297879946851	1.12E-1	0.195762381208	1.01E-2
5^3	0.133973629562	5.16E-2	0.170687175937	1.49E-2
7^3	0.205909568022	2.03E-2	0.187653409324	2.03E-3
16^3	0.185672156283	5.28E-5	0.185642045643	2.27E-5

TABLE 4

Comparison of accuracy between evaluating integral by direct Gauss quadrature and the regularization scheme. Reference solution: $g_{12} = 0.191817954$

M_A	Direct integration	Error	Regularization	Error
3^3	0.305344867573	1.14E-1	0.203232071458	1.14E-2
5^3	0.139964096534	5.19E-2	0.215028770323	2.32E-2
7^3	0.212156313739	2.03E-2	0.193901024185	2.10E-3
16^3	0.191870838667	5.28E-5	0.191840738376	2.28E-5

TABLE 5

Comparison of accuracy between evaluating integral by direct Gauss quadrature and the regularization scheme. Reference solution: $g_{22} = g_{33} = -0.092809645473$

M_A	Direct integration	Error	Regularization	Error
3^3	−0.148939973426	5.61E-2	−0.097881190604	5.10E-3
5^3	−0.066986814781	2.58E-2	−0.104520889503	1.17E-2
7^3	−0.102954784011	1.01E-2	−0.093826704662	1.01E-3
16^3	−0.092836078142	2.64E-5	−0.092821022821	1.14E-5

Tables 3–5 show the accuracy of calculating the matrix entries g_{11}, g_{12}, and g_{13} in (44) with and without the regularization scheme for M_A of Gaussian points. In these calculations, the reference solutions are computed with 32 ($M_A = 32^3$) Gaussian quadrature points in each direction. From the tables we can see that the results from the regularization scheme are more accurate than direct integration. Especially when the number of collocation points is 3^3 and 7^3, the accuracy is improved by one order of magnitude.

Next, we apply the proposed algorithm to compute the scattering of a MM with multiple meta-atom scatterers. Specifically, we consider the extreme (trivial) situation when the cubic meta-atom scatterers are adjacent to each other. This is done by dividing a single cube $[0, 2]^3$ into $N = h^3, h = 1, 2, 3, 4, 5, 6, 8$ cells. The solution of the VIE in each case is denoted as $\mathbf{E}^h$, and the solution $\mathbf{E}^8$ is taken as the reference solution. In order to handle a large number of scatters in realistic applications, only a small amount of collocation points in each cell is used. In this test, $M = 27$ collocation points are used in each cell. As shown in Figure 10, if no regularization scheme is applied, the solution of VIE will not converge to the reference solution when the cube is divided into smaller cells. In contrast, the VIE solution displays a convergence pattern when the regularization scheme is applied.

Cross sections of the VIE solution $\mathbf{E}^8$ at $z = 0.0281$ are shown in Figure 11, which lists the real parts of the solutions for E_z component. Figure 11(a) and 11(b) shows solving the VIE equation without and with the regularization scheme, respectively. In both cases, only 27 collocation points are used in each cell. Without the regularization scheme, this amount of Gaussian points is not enough to obtain an accurate

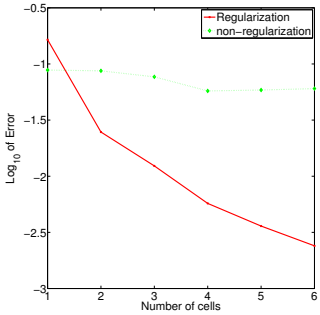

FIG. 10. *Convergence of the VIE solution in a cube* $[0,2]\times[0,2]\times[0,2]$ *divided into* $1\times1\times1$, $2\times2\times2$, $3\times3\times3$, $4\times4\times4$, $5\times5\times5$, *and* $6\times6\times6$ *cells, with* 27 *collocation points in each cell.*

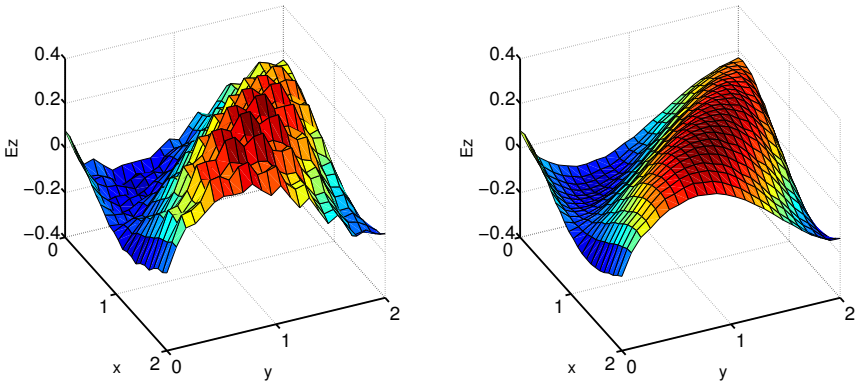

(a) (b)

FIG. 11. *VIE solutions for* E_z *in a cube at* $z = 0.0281$*:* (a) *without regularization scheme and* (b) *with regularization method.*

enough integral for matrix entries, so the resulting VIE solutions are spurious and not accurate. In contrast, if the regularization scheme is used, the resulting solution is smooth and gives convergence as shown in Figure 11. Similar phenomena are also found in E_x and E_y.

Comparing the results using regularization with $M_A = 3$, Tables 3–5 indicate that in order to obtain similar results without the regularization scheme, at least $7 \times 7 \times 7 = 343$ collocation points in each cells are needed, so the computation will be increased rapidly. Figure 12 summarizes the CPU time in the matrix filling process for a different number of M_A and a different number of cells. For $M = 27$ collocation points in each cell, it takes around 793 seconds to fill the matrix when there are 512 cells, but it will take 21,311 seconds when there are 343 collocation points in each cell. So the regularization scheme is important for a large number of meta-atoms.

It should be noted that the Lippmann–Schwinger equation for Maxwell equations is not a second kind of integral equation [17]; thus, the condition number of the matrix will grow with its size and the frequency of the incidence wave. In our current numerical examples, we consider up to 100 scatterers, and the frequency lies in the visible light range. Thus, the matrix size is moderate (up to 50,000×50,000), thanks to the special quadrature rules used in our method. In general, if possible, it is preferable

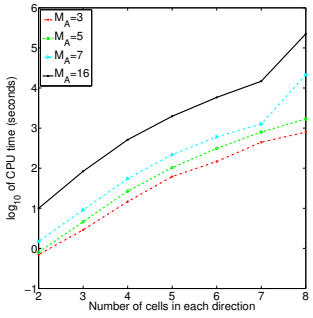

FIG. 12. *CPU time used in matrix filling process of solving the VIE solution with different number of Gaussian points.*

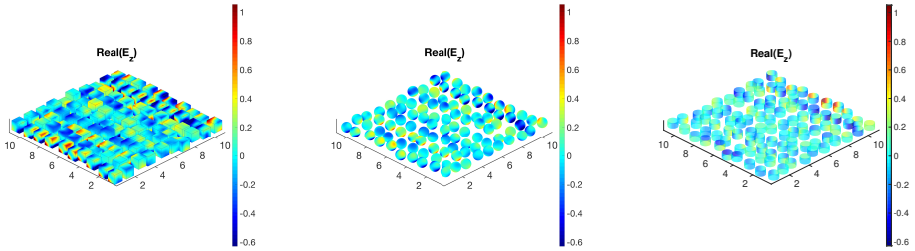

(a) (b) (c)

FIG. 13. *Electric field component E_z in 10×10 scatterer arrays with a TE incident wave in a half-space:* (a) *cubic scatterer with* 27 *collocation points in each,* (b) *spherical scatterer with* 72 *collocation points in each, and* (c) *cylindrical scatterer with* 72 *collocation points.*

to use a direct matrix solver rather than an iterative one for robust numerical results, such as the LU solver from LAPACK [2]. For a large number of scatterers with high frequencies in applications, iterative methods with proper preconditioners may be the only alternative, which will be studied in our future work. In our computations, an incomplete LU factorization preconditioned GMRES method from PETSc [5] is also used.

Finally, we calculate the reflection coefficients of a MM in a layered medium. As an example, we place an array of 10×10 cubes, balls, and cylinders on a dielectric boundary with $\epsilon_1 = 1, \mu_1 = 1$, and $\epsilon_2 = 6, \mu_2 = 1$, respectively. Each scatterer element is 100 nm in each dimension (cubes) or 100 nm in diameter (balls and cylinders). These scatterers are 15 nm apart while their positions are slightly perturbed. Then the VIE is solved with an incident wave in TE mode:

$$\mathbf{E}^{\text{inc}} = [0, e^{-i(k_x x + k_y y + k_z z)}, 0]^T, (k_x, k_y, k_z) = k(\sin\theta, 0, \cos\theta), \tag{45}$$

where θ is angle between the incident wave and the z-axis. Figure 13 displays the electric fields in meta-atoms for cubes (a), balls (b), and cylinders (c) with $\theta = \pi/4$, respectively.

The scattering field is calculated on a square surface with length 1.2 mm and 5 mm above those scatterers. The reflection coefficient is then calculated as the intensity ratio of the scattering field and the incident wave. Figure 14 shows the reflection coefficients against the incident angle in (a) and (b) and against the wavelength in

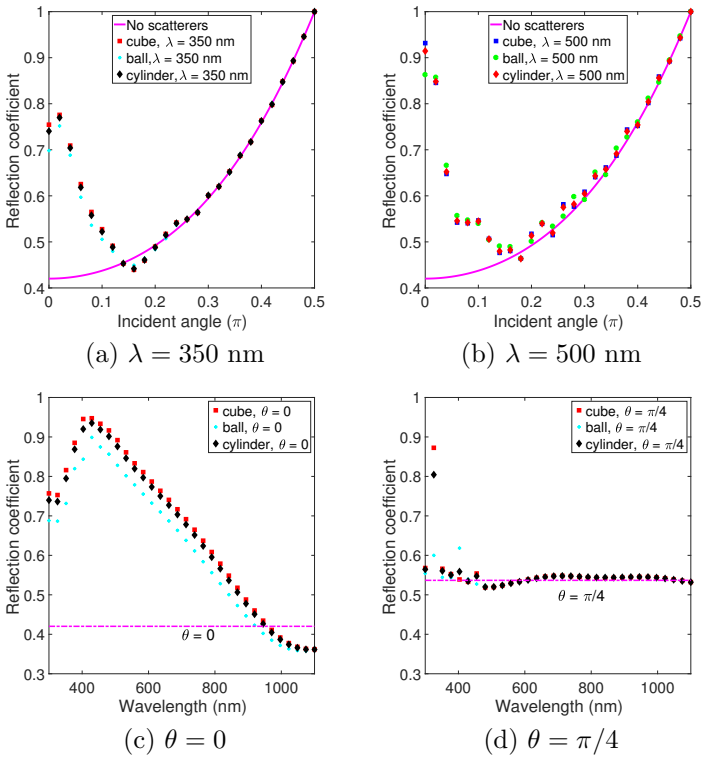

FIG. 14. *Reflection coefficients calculated from the VIE for* 3*-D MMs in a half-space:* (a) and (b) *against incident angle and* (c) and (d) *against wavelength of a TE incident wave.*

(c) and (d), respectively. In Figure 14(a) and 14(b), the reflection coefficients of the layered medium without scatterers are calculated by Fresnel's formulae and given in magenta. Reflection coefficients with cubic, spherical, or cylindrical scatterers at wavelengths $\lambda = 350$ nm and 500 nm are plotted as dots, respectively. In Figure 14(c) and 14(d), the angle of incident wave is fixed at 0 or $\pi/4$, and the corresponding reflection coefficients without scatterers are marked as dashed magenta lines for comparison. It can be concluded that 3-D meta-atoms contribute to more significant changes in reflection coefficients when the incident angles are smaller than $\pi/4$ or wavelengths are below 450 nm.

5. Conclusions. In this paper, we have presented an efficient numerical method based on a new volume integral equation of the Maxwell equations for the scattering of 3-D MMs in layered media. The VIE equation is formulated with the dyadic Green's functions for the layered media so that only the meta-atoms in the MMs need to be discretized. To address the difficulties of integrating the Green's functions in elements containing hypersingularities or high gradients, we split the dyadic Green's function into an analytic singular part in the form of free space Green's function and a smooth component. For the former, we treat the CPV using a finite exclusion volume together with some correction terms of removable singular integrals, both of which could be handled with a specially designed tensor-product quadrature. For the integrations in elements with high gradients, a regularization procedure is proposed converting volume integrals to surface integrals, which are amendable to analytic integration for

meta-atoms of cubes and spheres. For the smooth part of the dyadic Green's function in the physical space, a tabulation technique is also used to precompute various Hankel integrals, and an adaptive quadrature rule strategy is adopted to enhance computational efficiency. The proposed VIE method is validated by examining solution accuracy and computing the reflection coefficients of MMs of cubic, spherical, and cylindrical meta-atoms over a half-space. Future research will focus on fast solver for the VIE linear systems using preconditioned iterative methods.

Appendix A.

To derive the VIE for the layered medium, we take a small volume centered at $\mathbf{r}'$, $V_\delta = V_\delta(\mathbf{r}') \subset \Omega$, and the outward unit normal vectors of ∂V_δ and $\partial\Omega$ are labeled as $\mathbf{n}$ and $\mathbf{m}$, respectively. Normal directions of planar dielectric boundaries pointing upward are denoted as $\mathbf{n}_i, i = 1, 2, \ldots, N_l - 1$, as shown in Figure 2. Let the electric field $\mathbf{E}(\mathbf{r})$ in $\mathbb{R}^3$ be denoted by

$$\mathbf{E} = \begin{cases} \mathbf{E}^{\text{int}}(\mathbf{r}), & \mathbf{r} \in \Omega, \\ \mathbf{E}^{\text{inc}}(\mathbf{r}) + \mathbf{E}^{+}(\mathbf{r}), & \mathbf{r} \in \Omega^c \cap L_1, \\ \mathbf{E}_i^{-}(\mathbf{r}), & \mathbf{r} \in L_i, i = 2, 3, \ldots, N_l, \end{cases} \tag{46}$$

where $\mathbf{E}^{\text{int}}(\mathbf{r})$ is the electric field inside the scatterer Ω. The electric field in the air but outside the scatterer, namely, $\Omega^c \cap L_1$, consists of the incident wave $\mathbf{E}^{\text{inc}}(\mathbf{r})$, assumed to be a plane wave, and the reflected wave $\mathbf{E}^{+}(\mathbf{r})$. In the ith layer in the medium below S_1, the electric field is denoted as $\mathbf{E}_i^{-}(\mathbf{r})$. Overall, we have

$$\mathcal{L}\mathbf{E}(\mathbf{r}) - \omega^2 \epsilon_L \mathbf{E}(\mathbf{r}) = -i\omega \mathbf{J}_{eq}, \quad \mathbf{r} \in \Omega, \tag{47}$$

where $\mathbf{J}_{eq} = \mathrm{i}\omega\Delta\epsilon(\mathbf{r})\mathbf{E}^{\text{int}}(\mathbf{r})$ for $\mathbf{r} \in \Omega$ and $\mathbf{J}_{eq} = 0$ otherwise.

By multiplying (47) from the left by $\overline{\mathbf{G}}_{\mathbf{E}}$ and multiplying (2) from the right by $\mathbf{E}$ and taking the differences, we have

$$\mathcal{L}\mathbf{E} \cdot \overline{\mathbf{G}}_{\mathbf{E}} - \mathbf{E} \cdot \mathcal{L}\overline{\mathbf{G}}_{\mathbf{E}} = -i\omega \mathbf{J}_{eq} \cdot \overline{\mathbf{G}}_{\mathbf{E}} - \frac{1}{\mu(\mathbf{r})} \bar{\mathbf{I}} \mathbf{E} \delta(\mathbf{r} - \mathbf{r}'). \tag{48}$$

Integrating (48) on the domain $\mathbb{R}^3 \backslash V_\delta$, we have the following equation, after switching $\mathbf{r}$ and $\mathbf{r}'$:

$$\begin{aligned} -i\omega \int_{\Omega \backslash V_\delta} \mathbf{J}_{eq} \cdot \overline{\mathbf{G}}_{\mathbf{E}} d\mathbf{r}' &= \int_{\Omega \backslash V_\delta} d\mathbf{r}' (\mathcal{L}\mathbf{E}^{\text{int}} \cdot \overline{\mathbf{G}}_{\mathbf{E}} - \mathbf{E}^{\text{int}} \cdot \mathcal{L}\overline{\mathbf{G}}_{\mathbf{E}}) \\ &\quad + \int_{\Omega^c \cap L_1} d\mathbf{r}' (\mathcal{L}\mathbf{E}^{+} \cdot \overline{\mathbf{G}}_{\mathbf{E}} - \mathbf{E}^{+} \cdot \mathcal{L}\overline{\mathbf{G}}_{\mathbf{E}}) \\ &\quad + \sum_{i=2}^{N} \int_{L_i} d\mathbf{r}' (\mathcal{L}\mathbf{E}_i^{-} \cdot \overline{\mathbf{G}}_{\mathbf{E}} - \mathbf{E}_i^{-} \cdot \mathcal{L}\overline{\mathbf{G}}_{\mathbf{E}}) \\ &= I + II + III. \end{aligned} \tag{49}$$

Note that to obtain the second integral II on the right-hand side of (49), we have used the facts

$$\nabla \times \nabla \times \mathbf{E}^{\text{inc}} - \omega^2 \epsilon_1 \mathbf{E}^{\text{inc}} = 0 \quad \text{and} \quad \mathcal{L}\overline{\mathbf{G}}_{\mathbf{E}}(\mathbf{r}, \mathbf{r}') - \omega^2 \epsilon_L(\mathbf{r}) \overline{\mathbf{G}}_{\mathbf{E}}(\mathbf{r}, \mathbf{r}') = 0 \tag{50}$$

in the domain $\Omega^c \cap L_1$.

Using the vector-dyadic form of the Green's theorem, the first integral on the right-hand side of (49),

$$\begin{aligned} I = &- \int_{\partial V_\delta} \mathbf{n} \cdot \frac{1}{\mu} \left(\mathbf{E}^{\text{int}} \times \nabla \times \overline{\mathbf{G}}_{\mathbf{E}} + \nabla \times \mathbf{E}^{\text{int}} \times \overline{\mathbf{G}}_{\mathbf{E}} \right) ds' \\ &+ \int_{\partial \Omega} \mathbf{m} \cdot \frac{1}{\mu} \left(\mathbf{E}^{\text{int}} \times \nabla \times \overline{\mathbf{G}}_{\mathbf{E}} + \nabla \times \mathbf{E}^{\text{int}} \times \overline{\mathbf{G}}_{\mathbf{E}} \right) ds'. \end{aligned} \tag{51}$$

Similarly, the second integral II becomes

$$\begin{aligned} II = &- \int_{\partial \Omega} \mathbf{m} \cdot \frac{1}{\mu} \left(\mathbf{E}^{+} \times \nabla \times \overline{\mathbf{G}}_{\mathbf{E}} + \nabla \times \mathbf{E}^{+} \times \overline{\mathbf{G}}_{\mathbf{E}} \right) ds' \\ &- \int_{S_1} \mathbf{n}_1 \cdot \frac{1}{\mu} \left(\mathbf{E}^{+} \times \nabla \times \overline{\mathbf{G}}_{\mathbf{E}} + \nabla \times \mathbf{E}^{+} \times \overline{\mathbf{G}}_{\mathbf{E}} \right) ds' \\ &+ \int_{\partial \Gamma_\infty} \mathbf{n}_\infty \cdot \frac{1}{\mu} \left(\mathbf{E}^{+} \times \nabla \times \overline{\mathbf{G}}_{\mathbf{E}} + \nabla \times \mathbf{E}^{+} \times \overline{\mathbf{G}}_{\mathbf{E}} \right) ds', \end{aligned} \tag{52}$$

and the third integral becomes

$$\begin{aligned} III = &\int_{S_1} \mathbf{n}_1 \cdot \frac{1}{\mu} \left(\mathbf{E}_1^{-} \times \nabla \times \overline{\mathbf{G}}_{\mathbf{E}} + \nabla \times \mathbf{E}_1^{-} \times \overline{\mathbf{G}}_{\mathbf{E}} \right) ds' \\ &- \sum_{i=2}^{N-1} \int_{\partial \Omega} \mathbf{n}_i \cdot \frac{1}{\mu} \left(\mathbf{E}_i^{-} \times \nabla \times \overline{\mathbf{G}}_{\mathbf{E}} + \nabla \times \mathbf{E}_i^{-} \times \overline{\mathbf{G}}_{\mathbf{E}} \right) ds' \\ &+ \sum_{i=2}^{N-1} \int_{\partial \Omega} \mathbf{n}_i \cdot \frac{1}{\mu} \left(\mathbf{E}_{i+1}^{-} \times \nabla \times \overline{\mathbf{G}}_{\mathbf{E}} + \nabla \times \mathbf{E}_{i+1}^{-} \times \overline{\mathbf{G}}_{\mathbf{E}} \right) ds' \\ &+ \int_{\partial \Gamma_{-\infty}} \mathbf{n}_{-\infty} \cdot \frac{1}{\mu} \left(\mathbf{E}_N^{-} \times \nabla \times \overline{\mathbf{G}}_{\mathbf{E}} + \nabla \times \mathbf{E}_N^{-} \times \overline{\mathbf{G}}_{\mathbf{E}} \right) ds'. \end{aligned} \tag{53}$$

Summing up the integrals above and using the radiation boundary condition at infinity and continuity conditions of the electric field and Green's function on planar interfaces, we can simplify (49) to

$$\begin{aligned} -i\mu\omega \int_{\Omega \setminus V_\delta} \mathbf{J}_{eq} \cdot \overline{\mathbf{G}}_{\mathbf{E}} d\mathbf{r}' = &- \int_{\partial V_\delta} \mathbf{n} \cdot \left(\mathbf{E} \times \nabla \times \overline{\mathbf{G}}_{\mathbf{E}} + \nabla \times \mathbf{E} \times \overline{\mathbf{G}}_{\mathbf{E}} \right) ds' \\ &+ \int_{\partial \Omega} \mathbf{m} \cdot \left(\mathbf{E}^{\text{inc}} \times \nabla \times \overline{\mathbf{G}}_{\mathbf{E}} + \nabla \times \mathbf{E}^{\text{inc}} \times \overline{\mathbf{G}}_{\mathbf{E}} \right) ds' \\ &+ \int_{S_1} \mathbf{n}_1 \cdot \left(\mathbf{E}^{\text{inc}} \times \nabla \times \overline{\mathbf{G}}_{\mathbf{E}} + \nabla \times \mathbf{E}^{\text{inc}} \times \overline{\mathbf{G}}_{\mathbf{E}} \right) ds', \end{aligned} \tag{54}$$

where the superscript "int" has been dropped.

Next we will take the limit in (54) as $\delta \to 0$ after using the decomposition in (5). As shown in [8],

$$-\lim_{\delta \to 0} \int_{\partial V_\delta} \mathbf{n} \cdot \left(\mathbf{E} \times \nabla \times \overline{\mathbf{G}}_{\mathbf{E}}^{*} + \nabla \times \mathbf{E} \times \overline{\mathbf{G}}_{\mathbf{E}}^{*} \right) ds' = \mathbf{E}(\mathbf{r}) + i\mu\omega \mathbf{J}_{eq} \cdot \mathbf{L}_{V_\delta}, \tag{55}$$

where $\mathbf{L}_{V_\delta}$ is the V_δ shape-dependent dyadic whose formulations for various geometric shapes are given in [30], and we have $\mathbf{L}_{V_\delta} = \frac{1}{3}\mathbf{I}$ for a spherical exclusion volume.

On the other hand,

$$-\lim_{\delta\to 0}\int_{\partial V_\delta}\mathbf{n}\cdot\left(\mathbf{E}\times\nabla\times\overline{\mathbf{G}}_{\mathbf{E}}^{\mathrm{reg}}+\nabla\times\mathbf{E}\times\overline{\mathbf{G}}_{\mathbf{E}}^{\mathrm{reg}}\right)ds'=0 \tag{56}$$

since $\overline{\mathbf{G}}_{\mathbf{E}}^{\mathrm{reg}}$ is bounded.

Inserting (55) and (56) into (54) and recalling $\mathbf{J}_{eq}(\mathbf{r}) = i\omega\Delta\epsilon(\mathbf{r})\mathbf{E}(\mathbf{r})$, we obtain (4).

REFERENCES

[1] S. Ambikasaran, C. Borges, L.-M. Imbert-Gerard, and L. Greengard, *Fast, adaptive, high-order accurate discretization of the Lippmann–Schwinger equation in two dimensions*, SIAM J. Sci. Comput., 38 (2016), pp. A1770–A1787.

[2] E. Anderson, Z. Bai, C. Bischof, S. Blackford, J. Demmel, J. Dongarra, J. Du Croz, A. Greenbaum, S. Hammarling, A. McKenney, et al., *LAPACK Users' Guide*, Technical report, SIAM, 1999.

[3] H. Atwater, *The promise of Plasmonics*, Sci. Amer., (2007), pp. 56–62.

[4] H. Atwater and A. Polman, *Plasmonics for improved photovoltaic devices*, Nat. Mater., (2010), pp. 205–213.

[5] S. Balay, W. Gropp, L. C. McInnes, and B. F. Smith, *PETSc, the Portable, Extensible Toolkit for Scientific Computing*, Ver., 22, Argonne National Laboratory, 2 1998.

[6] A. Barnett and L. Greengard, *A new integral representation for quasi-periodic scattering problems in two dimensions*, BIT Numer. Math., 51 (2011), pp. 67–90.

[7] O. P. Bruno and A. G. Fernandez-Lado, *Rapidly convergent quasi-periodic Green functions for scattering by arrays of cylinders iincluding wood anomalies*, Proc. Roy. Soc. A, 473, (2017), p. 20160802.

[8] W. Cai, *Computational Methods for Electromagnetic Phenomena: Electrostatics in Solvation, Scattering, and Electron Transport*, Cambridge University Press, 2013.

[9] D. Chen, B. Zinser, W. Cai, and M. H. Cho, *Accurate and efficient Nyström volume integral equation method for the Maxwell equations for multiple 3-D scatterers*, J. Comput. Phys., (2016), pp. 303–320.

[10] W. C. Chew and W. H. Weedon, *A 3D perfectly matched medium from modified Maxwell's equations with stretched coordinates*, Microw. Opt. Technol. Lett., 7 (1994), pp. 599–604.

[11] M. H. Cho and A. H. Barnett, *Robust fast direct integral equation solver for quasi-periodic scattering problems with a large number of layers*, Opt. Express, 23 (2015), pp. 1775–1799.

[12] M. H. Cho and W. Cai, *Efficient and accurate computation of electric field dyadic Green's function in layered media*, J. Sci. Comput., 71 (2017), pp. 1319–1350.

[13] T. Cui and W. Chew, *Fast evaluation of Sommerfeld integrals for EM scattering and radiation by three-dimensional buried objects*, IEEE Trans. Geosci. Remote Sensing, (1999), pp. 887–900.

[14] Fikioris, *Electromagnetic field inside a current-carrying region*, J. Math. Phys., (1965), pp. 1617–1620.

[15] Y. Fu and X. Zhou, *Plasmonic lenses: A review*, Plasmonics, (2010), pp. 287–310.

[16] K. Hering, D. Cialla, K. Ackermann, T. Dörefer, R. Möller, H. Schneidewind, R. Mattheis, W. Fritzsche, P. Rösch, and J. Popp, *Plasmonic lenses: A review*, SERS: A Versatile Tool in Chemical and Biochemical Diagnostics, (2008), pp. 113–124.

[17] A. Kirsch and A. Lechleiter, *The operator equations of Lippmann–Schwinger type for acoustic and electromagnetic scattering problems in L^2*, Appl. Anal., 88 (2009), pp. 807–830.

[18] J. Kottmann and J. Martin, O, *Accurate solution of the Volume Integral Equation for high-permittivity scatters*, IEEE Trans. Antennas Propagation, (2000), pp. 1719–1726.

[19] G. Liu and S. Gedney, *High-order Nyström solution of the volume-EFIE for TE-wave scattering*, Electromagnetics, (2001), pp. 1–14.

[20] K. A. Michalski and J. R. Mosig, *Efficient computation of Sommerfeld integral tails—Methods and algorithms*, J. Electromagn. Waves Appl., 30 (2016), pp. 281–317.

[21] P. Monk, *Finite Element Methods for Maxwell's Equations*, Oxford University Press, 2003.

[22] J. Pendry, *Negative refraction makes a perfect lens*, Phy. Rev. Lett., (2000), pp. 3966–3969.

[23] H. Raether, *Surface Plasmons on Smooth and Rough Surfaces and Gratings*, Springer Tracts in Modern Physics, Springer, 1988.

[24] C. Raman and K. Krishnan, *A new type of secondary radiation*, Nature, (1928), p. 501.

[25] W. Shin and S. Fan, *Choice of the perfectly matched layer boundary condition for frequency-domain Maxwell's equations solvers*, J. Comput. Phys., 231 (2012), pp. 3406–3431.
[26] T. Søndergaard and B. Tromborg, *Lippmann-Schwinger integral equation approach to the emission of radiation by sources located inside finite-sized dielectric structures*, Phys. Rev. B, 66 (2002), p. 155309.
[27] F. L. Teixeira, *Time-domain finite-difference and finite-element methods for Maxwell equations in complex media*, IEEE Trans. Antennas Propagation, 56 (2008), pp. 2150–2166.
[28] M. Tong, Z. Qian, and W. Chew, *Nyström method solution of volume integral equations for electromagnetic scattering by 3D penetrable objects*, IEEE Trans. Antennas Propagation, (2010), pp. 1645–1652.
[29] S. C. Winton, P. Kosmas, and C. M. Rappaport, *FDTD simulation of TE and TM plane waves at nonzero incidence in arbitrary layered media*, IEEE Trans. Antennas Propagation, 53 (2005), pp. 1721–1728.
[30] A. Yaghjian, *Electric dyadic Green's functions in the source region*, Proc. IEEE, (1980), pp. 248–263.
[31] L. Ying, *Sparsifying preconditioner for the Lippmann–Schwinger equation*, Multiscale Model. Simul., 13 (2015), pp. 644–660.
[32] B. Zinser, W. Cai, and D. Chen, *Quadrature weights on tensor-product nodes for accurate integration of hypersingular functions over some simple 3-D geometric shapes*, Commun. Comput. Phys., (2016), pp. 1283–1312.